Atmos. Meas. Tech. Discuss., 8, 4489–4536, 2015
www.atmos-meas-tech-discuss.net/8/4489/2015/
doi:10.5194/amtd-8-4489-2015

Atmospheric Measurement Techniques Discussions

Next-generation angular distribution models for top-of-atmosphere radiative flux calculation from the CERES instruments: validation

W. Su[1], J. Corbett[2], Z. Eitzen[2], and L. Liang[2]

[1]MS420, NASA Langley Research Center, Hampton, Virginia, USA
[2]Science Systems & Applications, Inc., Hampton, Virginia, USA

Received: 8 April 2015 – Accepted: 9 April 2015 – Published: 4 May 2015

Correspondence to: W. Su (wenying.su-1@nasa.gov)

Published by Copernicus Publications on behalf of the European Geosciences Union.

Abstract

Radiative fluxes at the top of the atmosphere (TOA) from the Clouds and the Earth's Radiant Energy System (CERES) instrument are fundamental variables for understanding the Earth's energy balance and how it changes with time. TOA radiative fluxes are derived from the CERES radiance measurements using empirical angular distribution models (ADMs). This paper evaluates the accuracy of CERES TOA fluxes using direct integration and flux consistency tests. Direct integration tests show that the overall bias in regional monthly mean TOA shortwave (SW) flux is less than 0.2 $W m^{-2}$ and the RMS error is less than 1.1 $W m^{-2}$. The bias and RMS error are very similar between Terra and Aqua. The bias in regional monthly mean TOA LW fluxes is less than 0.5 $W m^{-2}$ and the RMS error is less than 0.8 $W m^{-2}$ for both Terra and Aqua. The accuracy of the TOA instantaneous flux is assessed by performing tests using fluxes inverted from nadir- and oblique-viewing angles using CERES along-track observations and temporally- and spatially-matched MODIS observations, and using fluxes inverted from multi-angle MISR observations. The TOA instantaneous SW flux uncertainties are about 2.3 % (1.9 $W m^{-2}$) over clear ocean, 1.6 % (4.5 $W m^{-2}$) over clear land, and 2.0 % (6.0 $W m^{-2}$) over clear snow/ice; and are about 3.3 % (9.0 $W m^{-2}$), 2.7 % (8.4 $W m^{-2}$), and 3.7 % (9.9 $W m^{-2}$) over ocean, land, and snow/ice under all-sky conditions. The TOA SW flux uncertainties are generally larger for thin broken clouds than for moderate and thick overcast clouds. The TOA instantaneous daytime LW flux uncertainties are 0.5 % (1.5 $W m^{-2}$), 0.8 % (2.4 $W m^{-2}$), and 0.7 % (1.3 $W m^{-2}$) over clear ocean, land, and snow/ice; and are about 1.5 % (3.5 $W m^{-2}$), 1.0 % (2.9 $W m^{-2}$), and 1.1 % (2.1 $W m^{-2}$) over ocean, land, and snow/ice under all-sky conditions. The TOA instantaneous nighttime LW flux uncertainties are about 0.5–1 % (< 2.0 $W m^{-2}$) for all surface types. Flux uncertainties caused by errors in scene identification are also assessed by using the collocated CALIPSO, CloudSat, CERES and MODIS data product. Errors in scene identification tend to underestimate TOA SW flux by about 0.6 $W m^{-2}$ and over-

AMTD
8, 4489–4536, 2015

estimate TOA daytime (nighttime) LW flux by 0.4 (0.2) Wm^{-2} when all CERES viewing angles are considered.

1 Introduction

The Clouds and the Earth's Radiant Energy System (CERES) instruments have been providing top of the atmosphere (TOA) radiative fluxes to the scientific community since the late 1990s, and have resulted in about 900 peer-reviewed journal publications with over 26 000 citations (as of October 2014). These fluxes have been instrumental in advancing our understanding of the effects of clouds and aerosols on radiative energy within the Earth–atmosphere system.

The CERES instrument consists of a three-channel broadband scanning radiometer (Wielicki et al., 1996). The scanning radiometer measures radiances in shortwave (SW, 0.3–5 µm), window (WN, 8–12 µm), and total (0.3–200 µm) channels at a spatial resolution of ~ 20 km at nadir. The longwave (LW) component is derived as the difference between total and SW channels. These measured radiances at a given sun–Earth-satellite geometry are converted to outgoing reflected solar and emitted thermal TOA radiative fluxes using CERES angular distribution models (ADMs).

Su et al. (2015) described the methodology used to develop the next-generation CERES ADMs, which were developed using the latest cloud algorithms (Minnis et al., 2010). These newly developed ADMs are used to produce the Edition 4 Single Satellite Footprint TOA/Surface Fluxes and Clouds (SSF) product for Terra and Aqua and Edition 1 SSF product for Suomi NPP, whereas fluxes in the Edition 2 and 3 SSF products are inverted using the ADMs described in Loeb et al. (2005). These ADMs are constructed using data taken in the rotating azimuth plane (RAP) scan mode. In this mode, the instrument scans in elevation as it rotates in azimuth, thus acquiring radiance measurements from a wide range of viewing combinations. Distinct ADMs are developed for different scene types, which are defined using a combination of variables (e.g., surface type, cloud fraction, cloud optical depth, cloud phase, aerosol optical

AMTD
8, 4489–4536, 2015

depth, precipitable water, lapse rate, etc.). Scene type classifications are based upon imager (Moderate Resolution Imaging Spectroradiometer (MODIS) on Terra and Aqua and Visible Infrared Imaging Radiometer Suite (VIIRS) on NPP) measurements within each CERES footprint. The CERES/MODIS and CERES/VIIRS cloud algorithms retrieve cloud fraction, cloud optical depth, cloud top and effective pressure/temperature (among other variables) for every MODIS and VIIRS pixel (Minnis et al., 2010). These pixel-level cloud properties are spatially and temporally matched with the CERES footprint, and are averaged over the CERES footprints by accounting for the CERES point spread function (PSF; Smith, 1994). Spectral radiances from MODIS and VIIRS observations are also averaged over CERES footprints weighted by the CERES PSF, and are used for scene type classifications. Meteorological fields used for scene type classifications are from the Global Modeling and Assimilation Office's Goddard Earth Observing System (GEOS) version 5.4.1 data assimilation system for CERES. This version provides consistent analysis over the entire CERES data record.

The main objective of this paper is to validate the TOA SW and LW fluxes inverted using the ADMs developed by Su et al. (2015). As there are no direct radiative flux measurements at the TOA, we have to rely on indirect approaches to assess the errors in the TOA SW and LW fluxes due to uncertainties in ADMs. We use the direct integration (DI) method (Suttles et al., 1992; Loeb et al., 2003, 2007) to assess the flux errors on a regional and global scale (Sect. 2). To assess the errors in instantaneous TOA fluxes, we rely on flux consistency tests between CERES and MODIS (Sect. 3) and among different MISR (Multi-angle Imaging SpectroRadiometer) cameras (Sect. 4). As ADMs depend on scene type, misclassification of scene type will lead to wrong selections of anisotropic factors and thus errors in the TOA fluxes. We take advantage of the merged CALIPSO, CloudSat, CERES, MODIS (C3M) data product (Kato et al., 2010) to assess the flux errors due to scene identification uncertainties (Sect. 5).

AMTD
8, 4489–4536, 2015

2 Regional mean TOA flux error: direct integration

2.1 Shortwave

The direct integration (DI) method constructs regional seasonal all-sky ADMs by directly integrating the CERES measured radiances from both cross-track and rotating azimuth plane measurements. Radiance measurements are composited over a region of 10° latitude × 10° longitude and over a three-month period to ensure the full range of viewing zenith (θ) and relative azimuth angle (ϕ) coverage needed for flux computation in a region. These ADMs are referred to as DI ADMs. However, the standard DI approach also requires uniform angular sampling in each region. This requires all portions of a 10° latitude × 10° longitude region contribute equally to the mean radiances in all angular bins. This requirement is problematic for CERES on Terra and Aqua, as their sun-synchronous orbits introduce a strong correlation between latitude and solar zenith angle (θ_0) and ϕ.

To overcome the limitation of the sun-synchronous orbit, the standard DI method was modified by constructing two sets of DI ADMs (Loeb et al., 2007). One set is based upon the CERES measured radiance (I_o) and the other set is based upon the ADM predicted radiance ($\hat{I}$). Doing so ensures that both sets of the DI ADMs have the same sampling coverage, as for each I_o, the CERES ADMs provide an $\hat{I}$. Fluxes inverted from these two sets of ADMs are compared, and the differences are assumed to be representative of the actual TOA flux error from uncertainties in the CERES ADMs.

The two sets of seasonal ADMs are applied to the cross-track data of the middle month of each season (i.e. January, April, July, and October) to calculate the instantaneous TOA fluxes for each 1°×1° grid box, though the DI ADMs have a spatial resolution of 10° × 10°. These gridded instantaneous fluxes are then converted to equivalent 24 h fluxes by applying a scaling factor determined from the ratio of the total daily insolation to the mean insolation at the satellites' overpass times. We then calculate the differences between these two sets of gridded 24 h fluxes and these differences are used to represent the uncertainty in the CERES monthly mean data product.

AMTD
8, 4489–4536, 2015

Figure 1 shows the monthly regional TOA SW flux error due to ADM uncertainties for 2002 CERES cross-track measurements on Terra. Here the flux error is defined as flux inverted from $\hat{I}$ DI ADMs minus flux inverted from I_o DI ADMs. The grey color indicates that the TOA SW flux error is less than 1 W m^{-2}, and about 86 % of the 1° × 1° grid boxes of the four months are shown in this color. There are about 5 % of the grid boxes that have a flux error greater than 2 W m^{-2}, and they are mostly over high latitude regions. The large uncertainties seen over the north of Greenland are due to snow identification errors. Some footprints over the glacier and rocky areas there are determined to be completely covered by a mixure of fresh and permanent snow. But it appears that these footprints are actually only partly covered by snow (especially in summer when the snow has melted). This means the ADM predicted radiance is much higher than the actual radiance, leading to the high uncertainties for the spring and summer seasons.

Table 1 summarizes the global monthly mean TOA SW flux biases and root-mean-square (RMS) errors for the four months we discussed in Fig. 1 along with those for CERES Aqua 2004. SW flux biases and RMS errors derived using the Edition 3 SSF data and ADMs developed by Loeb et al. (2005) are included (in parentheses) for comparison. The largest SW flux bias in the Edition 4 SSF is 0.2 W m^{-2} for July 2002, which is about half of the bias in the Edition 3 SSF. The RMS errors of Edition 4 SSF data are all smaller than those in Edition 3 SSF data. Comparison between the TOA SW flux errors derived using the Edition 4 SSF data and ADMs from Su et al. (2015) and using the Edition 3 SSF data and ADMs from Loeb et al. (2005) shows reduced biases for nearly all grid boxes with notable improvements over high latitude regions. The improved flux accuracy is a result of improvements made in scene type identification (Minnis et al., 2010) and in anisotropy characterization (Su et al., 2015).

2.2 Longwave

The TOA longwave (LW) flux is a weak function of solar zenith angle, thus the correlations between latitude and θ_0 and ϕ introduced by a sun-synchronous orbit have

AMTD
8, 4489–4536, 2015

a negligible effect on the sampling issue associated with the standard DI method. We use the standard DI method to assess the LW flux error by comparing the averaged ADM-derived TOA LW fluxes with the fluxes derived from direct integration. Regional mean TOA LW flux errors are determined separately for daytime ($\theta_0 \leq 90^\circ$) and nighttime ($\theta_0 > 90^\circ$). Then 24 h averaged TOA LW flux errors are determined by weighting the daytime and nighttime errors by fraction of daylight at each latitude for each month.

Figure 2 shows the regional distributions of TOA LW flux errors for the four months of 2002 using CERES Terra cross-track measurements. Here the flux error is defined as ADM-derived LW fluxes minus the DI LW fluxes. The TOA LW flux errors are less than 1 $W m^{-2}$ for about 87 % of the $1^\circ \times 1^\circ$ regions (shown in gray color). Only 1.2 % of the $1^\circ \times 1^\circ$ regions have flux errors greater than 2 $W m^{-2}$, and they are mostly located over the sea ice and the Antarctic permanent snow regions. Table 2 summarizes the global monthly mean TOA LW flux biases and RMS errors for CERES Terra 2002 and for CERES Aqua 2004. LW flux biases and RMS errors derived using the Edition 3 SSF data and the ADMs from Loeb et al. (2005) are also included for comparison. The TOA LW biases for the Edition 4 SSF are less than 0.5 $W m^{-2}$ and the RMS errors are less than 0.8 $W m^{-2}$ for all months. In comparison, the TOA LW biases in the Edition 3 SSF are slightly smaller than those in the Edition 4 SSF, but their RMS errors are similar. This indicates that the small biases seen in the Edition 3 SSF product are often a result of compensating error.

Table 3 summarizes the global monthly mean TOA WN flux biases and RMS errors for CERES Terra 2002 and for CERES Aqua 2004. WN flux biases and RMS errors derived using the Edition 3 SSF data and ADMs from Loeb et al. (2005) are also included for comparison. The comparison shows that the TOA WN flux biases in the Edition 4 SSF are slightly larger than those in the Edition 3 SSF and the RMS errors are fairly similar between them.

AMTD
8, 4489–4536, 2015

3 Instantaneous TOA flux consistency test between CERES and MODIS

As flux should be independent of the satellite viewing geometry, we use a consistency check, in which fluxes for the same footprint inverted from different viewing geometries are compared, to assess the accuracy of instantaneous flux due to uncertainties in anisotropy characterization. However, the consistency test is not a guarantee of absolute accuracy as it does not account for potential bias errors that are independent of viewing geometry (Loeb et al., 2003), such as scene identification errors.

CERES views the same footprint from different viewing angles, when operating in along-track mode. We choose not to directly compare fluxes inverted from different CERES angles, as the shape and size of the CERES footprints change with viewing zenith angle. Instead, we take advantage of the collocated MODIS pixels within a CERES footprint. The MODIS imager observes the same area as CERES within approximately 2 min, but from viewing zenith angles close to nadir. The MODIS pixel-level data are spatially and temporally matched with the CERES footprints, and are averaged over the CERES footprints by accounting for the CERES PSF. These CERES footprints are classified into 55 categories of cloud types, which are functions of cloud layer, cloud fraction, cloud optical depth, and cloud effective pressure (Table 4). Among them type 0 is for clear sky, types 1 to 27 are for single-layer cloud types, and types 28 to 54 are for multi-layer cloud types.

Narrowband radiances from MODIS channels of 0.65, 0.86, and 1.63 µm are converted to broadband shortwave radiance as follows:

$$I_{\mathrm{sw}}^{\mathrm{md}} = a_0 + a_1 I_{0.65} + a_2 I_{0.86} + a_3 I_{1.63}. \quad (1)$$

Narrowband radiance from the 11 µm MODIS channel is converted to broadband longwave radiance as follows:

$$I_{\mathrm{lw}}^{\mathrm{md}} = b_0 + b_1 I_{11}. \quad (2)$$

Regression coefficients ($a_i, i = 0,3$ and $b_i, i = 0,1$) are determined using collocated CERES cross-track near-nadir observations ($\theta < 10^{\circ}$) and MODIS observations. Re-

AMTD
8, 4489–4536, 2015

gressions are derived on a daily basis for each equal-area 1° latitude × 1° longitude region, and separate daytime and nighttime LW regressions are obtained. Only CERES footprints belonging to the dominant cloud type over the 1° × 1° region are included in the regression to minimize the narrowband-to-broadband regression errors caused by spectral changes for different cloud types (including clear, see Table 4). Only those regions that have a RMS error less than 3 % in SW narrowband-to-broadband conversion are included in the SW analysis, and the narrowband-to-broadband conversion errors are generally about 1 % for different cloud types. Over the clear ocean, footprints with a glint angle less than 40° are not included in the SW analysis. For LW, only those regions that have a RMS error less than 0.5 % in narrowband-to-broadband conversion are included in the analysis.

The "broadband" imager radiances ($I_{\mathrm{sw}}^{\mathrm{md}}$ and $I_{\mathrm{lw}}^{\mathrm{md}}$) are then converted to fluxes using the CERES shortwave and longwave ADMs and the MODIS viewing geometries. The near-nadir-viewing imager flux is then compared with the oblique-viewing ($50^{\circ} < \theta < 60^{\circ}$) CERES flux for the same footprint. Here we used 137 days of CERES along-track observations. For a population of N CERES footprints, the relative RMS error between fluxes $F(\theta_{\mathrm{i}}^{\mathrm{n}})$ inverted from near-nadir-viewing geometries and fluxes $F(\theta_{\mathrm{i}}^{\mathrm{o}})$ inverted from oblique-viewing geometries is used to quantify the TOA flux consistency:

$$\psi = \frac{\sqrt{\frac{1}{N}\sum_{i=1}^{N}\left[F\left(\theta_{\mathrm{i}}^{\mathrm{n}}\right) - F\left(\theta_{\mathrm{i}}^{\mathrm{o}}\right)\right]^2}}{\frac{1}{N}\sum_{i=1}^{N}F\left(\theta_{\mathrm{i}}^{\mathrm{o}}\right)} \times 100\,\%. \tag{3}$$

3.1 TOA SW flux consistency under clear conditions

We first examine the SW flux consistency for CERES clear footprints (cloud fraction < 0.1 %). Over ocean there are 22 137 clear CERES along-track footprints, and the relative RMS error is 4.1 % (3.4 W m^{-2}). Among these clear oceanic footprints, 20 298 have valid MODIS aerosol retrievals (Remer et al., 2008). To investigate whether ψ depends on aerosol optical depth (AOD), these footprints are sorted by AOD and then

AMTD
8, 4489–4536, 2015

divided into 10 bins, each with an equal number of samples. Figure 3 shows the mean oblique-view CERES fluxes and the relative RMS errors between the near-nadir-view and oblique-view fluxes for the 10 bins. As expected, the fluxes increase as AOD increases, but the relative RMS errors remain around 2.8 % for the first 9 bins and increase to about 6.6 % for the last bin. For this bin, AOD has a large range of values (from 0.19 to 1.74). This covers a large range of anisotropy that was not fully captured by the CERES clear-ocean ADMs, which were constructed for low-, mid-, and high-AOD bins (Su et al., 2015). Additionally, these large AOD retrievals are more likely to be affected by cloud contamination (Zhang and Reid, 2006), which can also increase the RMS error as the anisotropy under clear sky is different from that under cloudy sky.

To test if ψ depends on aerosol fine-mode fraction, we stratify the clear-ocean samples by AOD, θ_0, and MODIS fine-mode fraction. Figure 4 shows the relative RMS error ψ as a function of MODIS fine-mode fraction for four populations, and the occurrence frequency for each fine-mode fraction bin of each population. For the population with AOD < 0.1 and $\theta_0 < 50^\circ$, which consists of about 37.4 % of the total sample, the relative RMS errors are about 3–4 %. For the population with AOD < 0.1 and $\theta_0 > 50^\circ$, which consists of about 21.1 % of the total sample, the relative RMS errors are about 3 % except for one fine-mode fraction bin. For the population with AOD > 0.1 and $\theta_0 < 50^\circ$, which consists of about 28.8 % of the total sample, the relative RMS errors are about 3–5 %. For the population with AOD > 0.1 and $\theta_0 > 50^\circ$, the relative RMS errors are about 6–8 % for fine-mode fraction greater than 0.4, but these bins are only 7 % of the total population. These relative RMS errors are smaller than those presented in Loeb et al. (2007) and show less dependence on MODIS fine-mode fraction.

Over land there are 210 808 clear CERES along-track footprints, and the relative RMS error is 3.4 % (9 W m^{-2}). Among these footprints, 208 297 have valid MODIS dark target (Levy et al., 2010) or deep blue (Hsu et al., 2004) retrievals. For a given footprint, we use the AOD from the dark target retrieval if it is available, otherwise AOD from the deep blue retrieval is used. Similar to clear ocean, these clear footprints are sorted by AOD and then divided into 10 equal sample number bins. Figure 5a shows the

AMTD
8, 4489–4536, 2015

mean oblique-view CERES fluxes and the relative RMS errors for the 10 AOD bins. The relative RMS errors range from 2.8 to 4.4 % and do not show any dependence on AOD. We also examine the clear footprints over the Amazon region (0–30° S, 40–80° W). As the Amazon is very cloudy, we only have 3132 clear CERES along-track footprints with valid aerosol retrievals. Figure 5b shows the mean oblique-view CERES fluxes and the relative RMS errors for the 10 equal-sample-number bins. As the mean AOD increases from near zero (first bin) to about 0.55 (last bin), the relative RMS errors remain fairly constant (range between 3.3 to 5.1 %) and exhibit no dependence on AOD. This means that the CERES ADMs over clear land do not introduce an AOD-dependent flux uncertainty, as the relative RMS error is an indication of ADM uncertainty. This is in stark contrast to Patadia et al. (2011), in which their empirical ADMs produced a sharp jump of about 4 $W m^{-2}$ in SW flux at an AOD of 0.3. This unphysical jump in SW fluxes could be caused by the coarse angular resolution used by Patadia et al. (2011) and the fact that most of the angular bins for large AOD cases are based upon theoretical calculations.

3.2 TOA SW flux consistency under cloudy conditions

Figure 6 shows the instantaneous footprint-level relative RMS error of TOA SW flux (ψ, Eq. 3) for different cloud types (defined in Table 4) over ocean, land, and snow/ice. For each surface type, the top row is for high clouds, the middle row is for mid clouds, and the bottom row is for low clouds; the left column is for partly cloudy conditions, the middle column is for mostly cloudy conditions, and the right column is for overcast conditions. The narrow bars on the left are for single-layer cloud types and the wide bars on the right are for multi-layer cloud types. The color of the bar indicates the occurrence frequency of a cloud type. Due to data availability and RMS error restriction in narrowband-to-broadband conversion, we are not able to provide ψ for every cloud type.

Over ocean, the relative RMS error is larger under thin broken clouds than under moderate and thick overcast clouds. Overcast low clouds with moderate optical depth

AMTD
8, 4489–4536, 2015

have the highest occurrence frequency (23 %) over ocean and the relative RMS error for these clouds is around 3.5 % (11 W m^{-2}). The overall instantaneous SW fluxes are consistent to within 5.3 % (15 W m^{-2}) over ocean. Over land, only about 40 % of the CERES along-track footprints are cloudy. The relative RMS error is again larger under thin broken clouds than under moderate and thick overcast clouds, and the all-sky relative RMS error is 5.2 % (16 W m^{-2}). Over snow and ice, the relative RMS error is 3.0 % (8.8 W m^{-2}) under clear-sky conditions. Under cloudy conditions, the relative RMS error shows less dependence on cloud height and the all-sky relative RMS error is 6.7 % (18 W m^{-2}). The relative RMS errors for the multi-layer clouds are larger than those for the single-layer clouds over all three surface types, with the largest difference over ocean and the smallest difference over snow/ice. This could be caused by the parallax effect, as we used the surface as the reference level, or due to the fact that the ADMs were developed without separating single-layer clouds from multi-layer clouds. The relative RMS errors for clear ocean and clear land are smaller than those provided in Loeb et al. (2007), but the relative RMS errors for all-sky conditions are comparable. Large reductions in relative RMS errors are noted for both clear- and all-sky conditions over snow and ice, because of improved cloud algorithms and ADMs over polar regions (Su et al., 2015; Corbett and Su, 2015).

3.3 TOA LW flux consistency

Figures 7 and 8 show the instantaneous footprint-level relative RMS errors for daytime and nighttime TOA LW flux (ψ, Eq. 3) for different cloud types over three surface types. The daytime relative RMS errors are generally larger than the nighttime ones, possibly because the LW ADMs did not consider the effect of solar zenith angle and relative azimuth angle on anisotropy. Over ocean, the relative RMS errors are 0.9 % (2.5 W m^{-2}) and 0.8 % (2.3 W m^{-2}) for clear-sky daytime and nighttime footprints, whereas they are 2.5 % (5.9 W m^{-2}) and 1.3 % (3.3 W m^{-2}) for all-sky conditions. Over land, the relative RMS errors are 1.3 % (4.1 W m^{-2}) and 0.7 % (2.0 W m^{-2}) for clear-sky daytime and nighttime footprints, whereas they are 1.6 % (4.9 W m^{-2}) and 1.2 % (3.2 W m^{-2})

AMTD
8, 4489–4536, 2015

for all-sky conditions. Over snow and ice, the clear-sky relative RMS errors are 1.1 % (2.1 $W m^{-2}$) and 1.3 % (1.5 $W m^{-2}$) for daytime and nighttime footprints, and the all-sky relative RMS errors are 1.9 % (3.5 $W m^{-2}$) and 1.6 % (2.4 $W m^{-2}$) for daytime and nighttime footprints. The overall LW flux RMS errors reported here represent a 2–3 $W m^{-2}$ improvement compared to the results presented in Loeb et al. (2007). We also note that the relative RMS errors increase from low clouds to high clouds, although the amount that the error increases is smaller than that reported by Loeb et al. (2007). This reduction in error for high clouds is probably because the ADMs used here apply the mean observed radiance instead of the radiance derived from a third-order polynomial fit (Su et al., 2015), which improves the anisotropy characterization for high clouds.

3.4 TOA flux uncertainty

The relative RMS errors between fluxes derived from nadir- and oblique-viewing angles can be used to test how well the CERES ADMs characterize the anisotropy of the Earth scenes, but it is more important to provide the TOA flux uncertainty to the scientific community. The relationship between TOA flux relative RMS error and flux uncertainty is derived by using 1-dimensional and 3-dimensional radiative transfer calculations (Loeb et al., 2003, 2007; Kato et al., 2006). These calculations generate SW radiances and fluxes for liquid and ice clouds with optical depths between 0.1 and 200 using angular sampling from CERES Terra along-track SSF data. Idealized ADMs are used to estimate TOA fluxes from the radiances generated from the radiative transfer calculations. The relative RMS errors between nadir- and oblique-viewing zenith angles were compared with the corresponding TOA flux uncertainty determined from the difference between the actual fluxes from the radiative transfer calculations and the fluxes inverted from the idealized ADMs for all the scenes simulated. The ratio of TOA flux uncertainty to TOA flux relative RMS error ranges from 0.54 to 0.65, and the average is 0.60.

The average ratio is used here to convert the relative RMS error to flux uncertainty. Table 5 lists the clear-sky and all-sky SW, LW daytime and nighttime flux uncertainties

AMTD
8, 4489–4536, 2015

over different surface types. The TOA SW flux uncertainty is about 2 % under clear-sky conditions, as most of the clear land samples are over the highly reflective Sahara desert, resulting in an absolute flux uncertainty of about 5.8 $W m^{-2}$. Under all-sky conditions, the SW flux uncertainties are about 3–4 % (range from 9.0 to 10.7 $W m^{-2}$). For clear-sky TOA LW, the absolute flux uncertainty is less than 1.5 $W m^{-2}$ except for daytime land, as the emitting LW radiation over hot Saharan surfaces is greater than 300 $W m^{-2}$. Under all-sky conditions, the daytime LW flux uncertainties are less than 3.5 $W m^{-2}$ and the nighttime LW flux uncertainties are less than 2.0 $W m^{-2}$. These all-sky SW and LW flux uncertainties represent a 1–2 $W m^{-2}$ improvement from those obtained by Loeb et al. (2007).

4 Instantaneous multi-angle TOA SW flux consistency from MISR

The multi-angle and multi-channel radiances of the MISR Level 1B2 ellipsoid-projected data product are merged with the CERES Terra Edition 4 SSF data product by convolving the radiances from nine angles in four spectral bands with the CERES PSF, using a surface reference level. The details on the merged data set, referred to as SSFM, are provided in Loeb et al. (2006). As MISR instrument measures the radiances from nine along-track angles from nadir to ±70°, the merged data set provides extra information on the radiance anisotropy of each CERES footprint from nine spatially matched camera angles in the along-track direction.

For a given CERES footprint, the narrow-band MISR radiances at each of the nine MISR angles are converted to broadband SW radiances. This is accomplished by applying narrowband-to-broadband regression relationships that relate the MISR radiances in the blue (0.45 µm), red (0.67 µm), and near-infrared (0.87 µm) bands with a SW broadband radiance:

$$I_{sw}^{ms_j} = c_0 + c_1 I_{0.45} + c_2 I_{0.67} + c_3 I_{0.87}, \quad (4)$$

AMTD
8, 4489–4536, 2015

where $I_{0.45}$, $I_{0.67}$, and $I_{0.87}$ denote the MISR blue, red, and near-infrared radiances, and $I_{sw}^{ms_j}$ is the SW radiance for the jth MISR camera. Regression coefficients c_0, c_1, c_2, and c_3 are determined from coincident CERES SW and MISR narrow-band radiances using 107 days of merged SSFM product. Separate regressions are derived for predefined intervals of solar zenith angle, viewing zenith angle, relative azimuth angle, cloud fraction, effective cloud top pressure, precipitable water, and surface type. The sample numbers (N) required to minimize the narrow-to-broadband regression error are listed in Table for different surface types.

We then infer the TOA SW flux from $I_{sw}^{ms_j}$ for each of the MISR angles:

$$F_{sw}^{ms_j}(\theta_0) = \frac{\pi I_{sw}^{ms_j}(\theta_0, \theta_j, \phi_j)}{R(\theta_0, \theta_j, \phi_j)}, \tag{5}$$

where $R(\theta_0, \theta_j, \phi_j)$ is the CERES SW anisotropic factor corresponding to the scene types determined from MODIS measurements, and $\theta_0, \theta_j, \phi_j$ corresponds to the solar zenith angle, viewing zenith angle, and the relative azimuth angle of the MISR jth camera. Thus for each CERES footprint, we can have up to nine SW fluxes inferred from MISR measurements. The SD (σ) of these fluxes is used to measure the uncertainty of CERES ADMs. Only footprints with at least 5 valid MISR SW fluxes are included in this analysis. Over clear ocean and sea ice, MISR viewing angles that are within 15° of the specular direction are not included in this analysis. For a population of M CERES footprints, we examine the relative flux consistency by using the coefficient of variation, which is defined as:

$$\Psi_T = \frac{\sqrt{\frac{1}{M}\sum_{i=1}^{M}\sigma_i^2}}{\frac{1}{M}\sum_{i=1}^{M}\overline{F_i^{ms}}} \times 100\,\%, \tag{6}$$

where $\overline{F_i^{ms}}$ is the averaged TOA SW flux from all available MISR angles for the ith CERES footprint.

AMTD
8, 4489–4536, 2015

We assume two sources of uncertainties contribute to the relative consistency of the TOA SW fluxes (a third source will be addressed in Sect. 4.2). The first source is how well the CERES SW ADMs characterize the anisotropy for a given scene type, and the second source is how accurate the narrowband-to-broadband regressions are. The second uncertainty source is estimated by comparing the co-aligned CERES and MISR camera measurements (when their viewing zenith angles and relative azimuth angles are within 2°). We then determine the ADM error (Ψ_{ADM}) by subtracting the narrowband-to-broadband regression error (Ψ_{NB}) from the total error (Ψ_{T}), as in Loeb et al. (2006):

$$\Psi_{ADM} = \sqrt{\Psi_{T}^{2} - \Psi_{NB}^{2}}, \quad (7)$$

Ψ_{ADM} is used to assess the TOA SW flux consistency error due to uncertainties in CERES ADMs.

4.1 TOA SW flux consistency by cloud type

Figure 9 shows the TOA SW flux consistency error among the MISR camera angles over the three surface types. The narrow bars on the left are for single-layer cloud types and the wide bars on the right are for multi-layer cloud types (see Table 4). The height of the bar indicates the flux consistency error due to ADMs (Ψ_{ADM}) and the error bar indicates the contribution to the total consistency error from narrowband-to-broadband regressions. The color of the bar indicates the occurrence frequency of a cloud type.

Over ocean, single-layer low clouds account for 43 % of the cloudy scenes and Ψ_{ADM} is less than 4 % except for thin clouds under overcast conditions. Multi-layer low clouds account for 13 % of the cloudy scenes and Ψ_{ADM} is less than 7 %. For mid and high clouds, Ψ_{ADM} are generally larger than those for low clouds. Additionally, thin cloud types have larger Ψ_{ADM} compared to moderate and thick cloud types under most circumstances. Table 6 summarizes the TOA SW flux consistency error due to ADM uncertainties for clear-sky, single-layer clouds, multi-layer clouds, and all-sky conditions.

AMTD
8, 4489–4536, 2015

The SW fluxes are consistent to within 3.5 % (3.0 W m^{-2}) and 6.2 % (15.9 W m^{-2}) for clear-sky and all-sky conditions. For single-layer clouds the SW fluxes are consistent to within 4.6 % (12.7 W m^{-2}) and for multi-layer clouds the SW fluxes are consistent to within 8.4 % (20.2 W m^{-2}). These Ψ_{ADM} reported here represent a slight improvement compared to those presented in Loeb et al. (2006).

Over land, clear-sky footprints account for more than 60 % of the merged SSFM data, and Ψ_{ADM} is about 2.0 % (5.4 W m^{-2}) for these clear footprints. For single-layer clouds with occurrence frequency greater than 1 %, Ψ_{ADM} are mostly less than 4 %. We also observe that Ψ_{ADM} tends to increase as cloud height increases, and they are generally larger under thin cloud conditions than under moderate and thick cloud conditions. For single-layer clouds the SW fluxes are consistent to within 4.9 % (17.1 W m^{-2}) and for multi-layer clouds the SW fluxes are consistent to within 6.6 % (23.9 W m^{-2}). For all-sky conditions, the SW fluxes are consistent to within 4.0 % (11.8 W m^{-2}).

Over snow/ice, about 17 % of the merged SSFM footprints are clear and the Ψ_{ADM} is about 3.8 % (11.2 W m^{-2}). About 78 % of the cloudy footprints are single-layer clouds. For single-layer low and mid clouds, Ψ_{ADM} are less than 6 %, and increase slightly for high clouds but the increments are smaller than over ocean and land. The overall Ψ_{ADM} for single-layer clouds is 6.0 % (16.1 W m^{-2}), and the overall Ψ_{ADM} for multi-layer clouds is 6.1 % (15.6 W m^{-2}). For all-sky conditions, Ψ_{ADM} is 5.6 % (15.2 W m^{-2}).

4.2 Quantification of the parallax effect

The SW flux errors shown in Fig. 9 increase as the cloud height increases, and the increment is the largest over ocean and smallest over snow/ice. This could be partly caused by the parallax effect as MISR ellipsoid-projected radiances are referenced to the surface of the World Geodetic System 1984 (WGS84) ellipsoid. This means that for scenes with reflecting levels significantly above the ellipsoid level (i.e. mid- to high-cloud) the radiances from different camera angles could be originating from different

AMTD
8, 4489–4536, 2015

points, and potentially, different scene types. This can lead to incorrect ADM selection and artificially increasing Ψ_{ADM}.

To examine and attempt to quantify this effect, we developed a second SSFM dataset using the MISR Level 2 TOA/Cloud Stereo product (MIL2TCAL, Diner et al., 1999). The MIL2TCAL dataset contains MISR bi-directional reflectance (BRF) values that have been projected onto the reflecting-level reference altitude (RLRA). The projection is performed using the MISR cloud heights derived from co-registering the pixels from different cameras at the location of the reflecting level. The BRFs in this dataset are at a 2.2 km pixel size whereas the level 1 data are at a 1.1 km pixel size. In order to perform the convolution of the MISR pixels onto the CERES footprint, we first re-grid the level 2 BRFs onto a 1.1 km grid by assigning each of the four 1.1 km pixels within a 2.2 km pixel to be the value of that 2.2 km pixel. From this point we proceed as before with the convolution of the MISR level 2 pixels and CERES footprints.

One issue we encounter using the MISR Level 2 product is that the re-projection to the RLRA can result in pixels from oblique angles being obscured when clouds on either side of the pixel are higher than that pixel. These pixels are flagged as missing in the convolution process, reducing the percentage coverage. When we calculate Ψ_{ADM} using the Level 2 data as described above we only use footprints with MISR coverage greater than 99.9 %. This results in a discrepancy between the number of footprints processed using Level 1 and Level 2 MISR data. As such Ψ_{ADM} calculated using MISR Level 2 data will not be representative of the scenes included in Ψ_{ADM} calculated using MISR Level 1 data. To get a comparable estimate of the error using both MISR Level 1 and Level 2 data, we use a subset of the Level 1 data by requiring that for each CERES footprint at least five of the same MISR cameras have valid radiances for both Level 1 and Level 2 data, and both Level 1 and Level 2 data have greater than 99.9 % coverage. This matched Level 1 and Level 2 dataset is used to estimate the parallax effect.

AMTD
8, 4489–4536, 2015

For the MISR Level 1 data, we now expand the total error into three error sources (ADM, narrowband-to-broadband regression, and parallax):

$$\Psi_T^2 = \Psi_{ADM}^2 + \Psi_{NB}^2 + \Psi_{PX}^2; \quad (8)$$

while for the MISR Level 2 data, we assume the parallax effect is negligible, thus the total error is composed of only errors from ADM and narrowband-to-broadband regression:

$$\Psi_T'^2 = \Psi_{ADM}^2 + \Psi_{NB}^2. \quad (9)$$

The difference between these two equations allow us to quantify the parallax effect as:

$$\Psi_{PX} = \sqrt{\Psi_T^2 - \Psi_T'^2}. \quad (10)$$

As the matching criteria used for MISR Level 1 and Level 2 data bias the footprints to homogenous scenes, the parallax effect reported here should be considered as the lower bound of the parallax effect. The ADM errors derived with the subset MISR Level 1 data are indeed smaller than those derived with the full Level 1 data, supporting the hypothesis that scenes included in the subset are more homogenous. Note the matched MISR data are only used to derive Ψ_{PX}, whereas Ψ_{ADM} is derived using the full Level 1 data.

Over oceans, the parallax effect Ψ_{PX} is 1.7 and 3.3 % for single-layer low and high clouds, and is 2.4 and 3.7 % for multi-layer low and high clouds. The parallax effect is indeed larger for high clouds than for low clouds. Considering all single-layer (multi-layer) clouds, the parallax effect is estimated to be 2.2 % (2.8 %); this results in a parallax effect of about 2.3 % under all-sky conditions. Taking these parallax effects into account, the flux consistency due to ADM uncertainty (using full MISR Level 1 data) is reduced to about 5.8 % for all-sky, 4.1 and 7.9 % for single- and multi-layer clouds (Table).

Over land, the parallax effect is fairly small under all-sky conditions (0.9 %) as most of the footprints in SSFM are clear (which are not affected by the parallax effect). For

AMTD
8, 4489–4536, 2015

single-layer clouds the parallax effect is about 2.7 %, and it is larger for high clouds (3.0 %) than for low clouds (0.8 %). For multi-layer clouds, the parallax effect is 3.4 %, and it is also larger for high clouds (3.8 %) than for low clouds (1.7 %). Taking these parallax effects into account, Ψ_{ADM} is reduced to 4.1 % for single layer clouds, and 5.7 % for multi-layer clouds.

Over snow/ice, the parallax effect is small for all cases (~ 0.7 %). This is not surprising, as the differences in anisotropy between clouds and snow/ice are fairly small, and misidentification of scenes between snow/ice and clouds has a small effect on flux inversion.

As discussed in Sect. 3.4, the ratio of TOA flux uncertainty to TOA flux consistency error is 0.6. We apply this ratio to convert the MISR flux consistency error (after removing the parallax effect) to TOA flux uncertainty under different conditions (see Table 7). The flux uncertainties presented here are consistent with the SW flux uncertainties based upon the CERES-MODIS consistency test (Table 5). Under clear-sky conditions, the instantaneous TOA SW flux has an uncertainty of about 2–3 $W m^{-2}$ over ocean and land, and about 7 $W m^{-2}$ over snow/ice. Under all-sky conditions, the instantaneous flux uncertainty is about 7–9 $W m^{-2}$. The instantaneous flux uncertainty for multi-layer cloudy scenes is larger than that for single-layer cloudy scenes over ocean and land, but they are similar over snow/ice.

5 Flux uncertainty from scene identification error

The merged CALIPSO, CloudSat, CERES, MODIS (C3M) data product (Kato et al., 2010) provides coincident "standard" CERES-MODIS cloud property retrievals over the CloudSat and CALIPSO ground track, and "C3M-enhanced" cloud property retrievals using cloud mask and height information from CALIPSO and CloudSat. Each of the two sets of cloud properties can be used to obtain a TOA flux estimate with the CERES observed SW and LW radiances and the anisotropic factors associated with the cloud properties. Note that the observed radiance is measured from the en-

AMTD
8, 4489–4536, 2015

tire footprint; therefore, there is a possible mismatch between the conditions over the ground-track portion of each footprint used here and the conditions over the footprint as a whole. However, the standard and C3M-enhanced ground-track cloud masks provide the only direct comparison between cloud masks, since there is no C3M-enhanced cloud mask available over the entire CERES footprint.

When the TOA fluxes determined using the C3M-enhanced cloud properties are compared to the fluxes determined using the standard CERES-MODIS cloud properties, the difference is used as a measure of uncertainty due to errors in scene identification (assuming C3M-enhanced cloud properties are the truth and the ground-track is representative of the whole footprint). Here, we use four seasonal months (January, April, July, and October 2010) of C3M data, in which the standard CERES-MODIS cloud property retrievals are based upon the cloud algorithms developed for Edition 4 SSF (Minnis et al., 2010; Chang et al., 2010; Sun-Mack et al., 2014).

5.1 Shortwave

Cloud fraction (f), cloud optical depth (τ), cloud phase, surface type, and spectral radiances from MODIS measurements are used to select the SW anisotropic factors for radiance-to-flux conversion. Figure 10a shows the four-seasonal-month mean TOA SW flux differences using scene identifications from the standard and enhanced cloud algorithms. The global mean flux difference is $-1.8\,\mathrm{W\,m^{-2}}$ and the largest regional differences of $-8\,\mathrm{W\,m^{-2}}$ are seen over sea ice. The cause for the flux difference is solely from the differences in anisotropic factors selected from the standard and the enhanced cloud algorithms. The standard cloud algorithm tends to miss thin clouds, which have smaller SW anisotropic factors than thicker clouds at the near-nadir viewing geometries that are included in the C3M data product. Consequently, fluxes inverted using scene identifications from the enhanced cloud algorithm are larger than those using scene identifications from the standard cloud algorithm over most regions.

The C3M product only includes CERES footprints that are coincident with CALIPSO ground track, thus only near-nadir viewing CERES footprints are considered. The $1^\circ \times 1^\circ$

AMTD
8, 4489–4536, 2015

grid averaged viewing zenith angle distributions for April 2010 are shown in Fig. 11, the grid averaged viewing zenith angles included in C3M are all smaller than 20°, whereas the CERES instrument samples a much wider range of viewing zenith angles. As a result the flux uncertainty shown in Fig. 10a is only representative of the near-nadir viewing CERES footprints.

The CERES SW anisotropic factors have a strong dependence on viewing zenith angle. For example, the anisotropic factors for clouds with $\ln(f\tau) = 6$ are smaller than the anisotropic factors for clouds with $\ln(f\tau) = 7$ for small viewing zenith angles, but the reverse is true for large viewing zenith angles (see Figs. 5a and 9a in Su et al., 2015). Thus, misclassification of scenes can result in either overestimation or underestimation of anisotropic factors depending on the viewing zenith angle, which leads to underestimation or overestimation of the TOA fluxes depending on the viewing zenith angle. It is therefore desirable to assess the flux uncertainty using a realistic CERES viewing zenith angle distribution (blue line in Fig. 11). To accomplish this, we assume the near-nadir viewing cloud property differences between the standard algorithm and the enhanced algorithm are representative for the whole CERES swath (covers about 24° longitude). We then repeat the flux calculation using all CERES viewing geometries sampled for each 0.2° latitude by 24° longitude bin for each day. We choose this bin size as it produces the most realistic daily grid-average viewing zenith angle distribution (red line in Fig. 11). Figure 10b shows the TOA SW flux differences accounting for the "realistic" CERES viewing geometries. The global monthly mean difference is reduced to $-0.6\,\mathrm{W\,m^{-2}}$, because thin clouds have larger anisotropic factors than thick clouds for oblique viewing zenith angles, thus partly compensating the flux differences when only near-nadir viewing zenith angles are considered. There are 59.3 % of the $1° \times 1°$ regions have a flux difference less than $1\,\mathrm{W\,m^{-2}}$ and 81.8 % of the regions have a flux difference less than $2\,\mathrm{W\,m^{-2}}$.

AMTD
8, 4489–4536, 2015

5.2 Longwave

Cloud fraction, cloud top temperature, visible cloud optical depth, ice/liquid water effective sizes, surface skin temperature, precipitable water, and lower-tropospheric lapse rate (measured over the lowest 300 hPa) are used to select the LW anisotropic factors. Figure 12a and c show the four-seasonal-month mean daytime and nighttime TOA LW flux differences using scene identifications from the standard and enhanced cloud algorithms. The global mean flux difference is 0.8 and 0.3 $W m^{-2}$ for daytime and nighttime, respectively. The largest regional differences are up to 5 $W m^{-2}$, and are observed over land during daytime. The flux differences are caused by the cloud property differences between the standard and the enhanced cloud algorithms, as the standard cloud algorithm misses thin clouds, which have larger LW anisotropic factors than thick clouds at the near-nadir viewing geometries that are included in the C3M data product (see Fig. 16b in Su et al., 2015). As a result, fluxes inverted using scene identifications from the enhanced cloud algorithm are smaller than those using scene identifications from the standard cloud algorithm over most regions.

The CERES LW anisotropic factors decrease as viewing zenith angle increases (limb darkening), and the anisotropic factors for thin clouds decrease faster than for thick clouds. As shown in Fig. 16b of Su et al. (2015), the anisotropic factors for thin clouds (dashed line) are larger than the anisotropic factors for thick clouds (solid line) for small viewing zenith angles but are smaller for large viewing zenith angles. To account for all viewing angles sampled by the CERES instrument, we use the same method as outlined in the SW section to extend the LW flux error caused by scene identification uncertainties to all CERES viewing geometries. Figure 12b and d show the TOA LW flux errors accounting for all CERES viewing geometries for daytime and nighttime. The global monthly mean differences are reduced to 0.4 and 0.2 $W m^{-2}$, because the LW anisotropic factors for thin clouds are smaller than those for thick clouds for oblique viewing angles, thus offset the flux difference when only near-nadir viewing angles are

AMTD
8, 4489–4536, 2015

included. There are 91.0 and 98.1 % of daytime and nighttime 1° × 1° regions that have a flux difference less than 1 W m^{-2}.

Here we have only addressed the flux uncertainty from scene identification errors that affect the selection of anisotropic factors used in radiance-to-flux conversion. Scene identification errors could also cause misclassifications of scenes used in building the CERES ADMs. However, we do not have enough data to assess the ADM uncertainties from scene identification errors.

6 Conclusions

We evaluated the TOA flux errors caused by the uncertainties in CERES ADMs that were recently developed using all available CERES RAP measurements (Su et al., 2015). This set of ADMs are used to produce the CERES Edition 4 SSF data product for Terra and Aqua and Edition 1 SSF data product for Suomi NPP. The TOA fluxes from CERES measurements are fundamental for studying the Earth's radiation budget and quantifying the uncertainties associated with these fluxes is critical in many applications of the CERES fluxes.

We have used the modified direct integration method, in which fluxes inverted from regional (10° × 10°) seasonal all-sky ADMs constructed using observed radiances and CERES ADM-predicted radiances are compared to assess the regional monthly mean TOA SW flux uncertainty. The biases in regional monthly mean TOA SW fluxes are less than 0.2 W m^{-2} and the RMS error are less than 1.1 W m^{-2}. The biases and RMS errors are very similar between Terra and Aqua. The regional monthly mean TOA LW flux uncertainty is assessed using the standard direct integration method, in which ADM-derived TOA LW fluxes are compared with the fluxes derived from regional seasonal all-sky ADMs constructed by directly integrating the CERES measured radiances. The biases in regional monthly mean TOA LW fluxes are less than 0.5 W m^{-2} and the RMS errors are less than 0.8 W m^{-2} for both Terra and Aqua.

AMTD
8, 4489–4536, 2015

A series of consistency tests were performed to evaluate the instantaneous TOA flux uncertainties. The consistency test is based upon the fact that flux is independent of the satellite's viewing angle, thus difference in fluxes inverted from different viewing angles for the same footprint are used to assess the instantaneous flux uncertainty. We have performed consistency tests using fluxes inverted from nadir- and oblique-viewing angles using CERES along-track observations and temporally- and spatially-matched MODIS observations. Over clear ocean, the SW fluxes are consistent to within 4.1 % (3 W m^{-2}) and show very little dependence on aerosol optical depth when it is less than 0.2. Furthermore, the flux consistency shows a much smaller dependence on aerosol fine mode fraction than previously reported (Loeb et al., 2007). Over clear land, the SW fluxes are consistent to within 3.4 % (9 W m^{-2}) and again show nearly no dependence on aerosol optical depth. Under all-sky conditions, the SW fluxes are consistent to within 5.3 % (15 W m^{-2}), 5.2 % (16 W m^{-2}), and 6.7 % (18 W m^{-2}) over ocean, land, and snow/ice surfaces. The LW fluxes are consistent to within 1.3 % (1.3 to 4.1 W m^{-2}) under clear conditions. Under all-sky conditions, the LW fluxes are consistent to within between 1.2 and 2.5 % (2.4–5.9 W m^{-2}) over different surfaces.

Another consistency test was performed by collocating CERES Terra measurements with MISR observations. Fluxes inverted from the nine MISR camera angles are used to assess the TOA SW flux uncertainty. MISR Level 1 and Level 2 data are compared to estimate the parallax effect, which is larger for high clouds than for low clouds. The parallax effect estimated here should be regarded as the lower bound, as the matching criteria we used tend to favor the more homogenous scenes. The parallax effect is about 2.3, 0.9, and 0.7 % over ocean, land, and snow/ice. Over ocean, the SW fluxes are consistent to within 3.5 % (3.0 W m^{-2}) and 5.8 % (14.9 W m^{-2}) under clear- and all-sky conditions due to ADM uncertainties. Over land, the SW fluxes are consistent to within 2.0 % (5.4 W m^{-2}) and 3.9 % (11.5 W m^{-2}) under clear- and all-sky conditions due to ADM uncertainties. Over snow/ice, the SW fluxes are consistent to within 3.8 % (11.2 W m^{-2}) and 5.6 % (15.2 W m^{-2}) under clear- and all-sky conditions.

AMTD
8, 4489–4536, 2015

The TOA flux consistency is converted to TOA flux uncertainty by a factor of about 0.6, which is derived based upon radiative transfer simulations (Loeb et al., 2007). The TOA instantaneous SW flux uncertainties are about 1.9 $W m^{-2}$ over clear ocean, 4.5 $W m^{-2}$ over clear land, and 6.0 $W m^{-2}$ over clear snow/ice; and are about 9.0, 8.4, and 9.9 $W m^{-2}$ over ocean, land, and snow/ice under all-sky conditions. The TOA instantaneous daytime LW flux uncertainties are 1.5, 2.4, and 1.3 $W m^{-2}$ over clear ocean, land, and snow/ice; and are about 3.5, 2.9, and 2.1 $W m^{-2}$ over ocean, land, and snow/ice under all-sky conditions. The TOA instantaneous nighttime LW flux uncertainties are smaller than 2.0 $W m^{-2}$ for all surface types.

As the CERES ADMs are scene type dependent, we also assessed the flux uncertainties caused by errors in scene identification using collocated CALIPSO, CloudSat, CERES and MODIS (C3M) data product. Only near-nadir-viewing CERES footprints are included in the C3M product. Errors in scene identification tend to underestimate the TOA SW flux by about 1.8 Wm^{-2} when only near-nadir-viewing CERES footprints are used. As the anisotropic factors depend on viewing zenith angle, we extended this evaluation to all viewing zenith angles by assuming the near-nadir-viewing scene identification errors are representative of the whole CERES swath. The underestimation is reduced to 0.6 Wm^{-2} after the comparison is extended to represent a realistic CERES viewing zenith angle distribution. Errors in scene identification tend to overestimate TOA daytime (nighttime) LW flux by about 0.8 (0.3) Wm^{-2} when only near-nadir-viewing CERES footprints are used, and the overestimation is reduced to 0.4 (0.2) Wm^{-2} after the comparison is extended to represent a realistic CERES viewing zenith angle distribution.

The CERES team has developed direct integration and various consistency tests to evaluate the accuracies of the TOA fluxes inverted by using the empirical ADMs, because of the lack of direct flux measurements at the TOA. The consistency tests show that the flux uncertainties for multi-layer clouds and high clouds are larger than for single-layer clouds and low clouds, point to the need to further evaluate the ADMs for those cases and will be addressed in the future development of CERES ADMs.

AMTD
8, 4489–4536, 2015

Furthermore, CERES Aqua ADMs are used to derive fluxes from radiances measured by CERES instrument on Suomi NPP. As the altitude of Suomi NPP orbit is higher than that of Aqua, the footprint size of CERES instrument on Suomi NPP is larger than that on Aqua. Will the difference in footprint size cause any uncertainties in Suomi NPP fluxes? Additionally the channels on VIIRS are different from the channels on MODIS, which can result in differences in retrieved cloud properties and affect the selections of ADMs used for flux inversion. Evaluations of these issues are currently under way and will be addressed in a future publication.

Acknowledgements. The authors thank Norman Loeb, Patrick Minnis, Walter Miller, Seiji Kato for helpful discussions.

References

Chang, F.-L., Minnis, P., Ayers, J. K., McGill, M. J., Palikonda, R., Spangenberg, D. A., Smith, W. L., and Yost, C. R.: Evaluation of satellite-based upper troposphere cloud top height retrieval in multilayer cloud conditions during TC4, J. Geophys. Res., 115, D00J05, doi:10.1029/2009JD013305, 2010. 4509

Corbett, J. and Su, W.: Corbett, J. and Su, W.: Accounting for the effects of Sastrugi in the CERES Clear-Sky Antarctic shortwave ADMs, Atmos. Meas. Tech. Discuss., 8, 375–404, doi:10.5194/amtd-8-375-2015, 2015. 4500

Diner, D. J., Davies, R., Di Girolamo, L., Horvath, A., Moroney, C., Muller, J.-P., Paradise, S. R., Wenkert, D., and Zong, J.: Level 2 Cloud Detection and Classification Algorithm Theoretical Basis, Tech. Rep. D-11399, JPL, 1999. 4506

Hsu, C., Tsay, S., King, M. D., and Herman, M.: Aerosol properties over bright-reflecting source regions, IEEE T. Geosci. Remote, 42, 557–569, 2004. 4498

Kato, S., Hinkelman, L. M., and Cheng, A.: Estimate of satellite-derived cloud optical thickness and effective radius errors and their effect on computed domain-averaged irradiances, J. Geophys. Res., 111, D17201, doi:10.1029/2005JD006668, 2006. 4501

Kato, S., Sun-Mack, S., Miller, W. F., Rose, F. G., Chen, Y., Minnis, P., and Wielicki, B. A.: Relationships among cloud occurrence frequency, overlap, and effective thickness derived

AMTD
8, 4489–4536, 2015

from CALIPSO and CloudSat merged cloud vertical profiles, J. Geophys. Res., 115, D00H28, 2010. 4492, 4508

Levy, R. C., Remer, L. A., Kleidman, R. G., Mattoo, S., Ichoku, C., Kahn, R., and Eck, T. F.: Global evaluation of the Collection 5 MODIS dark-target aerosol products over land, Atmos. Chem. Phys., 10, 10399–10420, doi:10.5194/acp-10-10399-2010, 2010. 4498

Loeb, N. G., Loukachine, K., Manalo-Smith, N., Wielicki, B. A., and Young, D. F.: Angular distribution models for top-of-atmosphere radiative flux estimation from the clouds and the Earth's radiant energy system instrument on the tropical rainfall measuring mission satellite. Part II: Validation, J. Appl. Meteorol., 42, 1748–1769, 2003. 4492, 4496, 4501

Loeb, N. G., Kato, S., Loukachine, K., and Manalo-Smith, N.: Angular distribution models for top-of-atmosphere radiative flux estimation from the Clouds and the Earth's Radiant Energy System instrument on the Terra satellite. Part I: Methodology, J. Atmos. Ocean. Tech., 22, 338–351, 2005. 4491, 4494, 4495, 4518, 4519, 4520

Loeb, N. G., Sun, M., Miller, W. F., Loukachine, K., and Davies, R.: Fusion of CERES, MISR, and MODIS measurements for top-of-atmosphere radiative flux validation, J. Geophys. Res., 111, D18209, doi:10.1029/2006JD007146, 2006. 4502, 4504, 4505

Loeb, N. G., Kato, S., Loukachine, K., Manalo-Smith, N., and Doelling, D. R.: Angular distribution models for top-of-atmosphere radiative flux estimation from the Clouds and the Earth's Radiant Energy System instrument on the Terra satellite. Part II: Validation, J. Atmos. Ocean. Tech., 24, 564–584, 2007. 4492, 4493, 4498, 4500, 4501, 4502, 4513, 4514

Minnis, P., Sun-Mack, S., Trepte, Q. Z., Chang, F.-L., Heck, P. W., Chen, Y., Yi, Y., Arduini, R. F., Ayers, K., Bedka, K., Bedka, S., and Brown, R.: CERES edition 3 cloud retrievals, in: 13th Conference on Atmospheric Radiation, Am. Meteorol. Soc., Oregon, Portland, 2010. 4491, 4492, 4494, 4509

Patadia, F., Christopher, S. A., and Zhang, J.: Development of empirical angular distribution models for smoke aerosols: methods, J. Geophys. Res., 116, D14203, doi:10.1029/2010JD015033, 2011. 4499

Remer, L. A., Kleidman, R. G., Levy, R. C., Kaufman, Y. J., Tanre, D., Mattoo, S., Martins, J. V., Ichoku, C., Koren, I., Yu, H., and Holben, B.: Global aerosol climatology from the MODIS satellite sensors, J. Geophys. Res., 113, D14S07, doi:10.1029/2007JD009661, 2008. 4497

Smith, G. L.: Effects of time response on the point spread function of a scanning radiometer, Appl. Optics, 33, 7031–7037, 1994. 4492

AMTD
8, 4489–4536, 2015

Su, W., Corbett, J., Eitzen, Z., and Liang, L.: Next-generation angular distribution models for top-of-atmosphere radiative flux calculation from CERES instruments: methodology, Atmos. Meas. Tech., 8, 611–632, doi:10.5194/amt-8-611-2015, 2015. 4491, 4492, 4494, 4498, 4500, 4501, 4510, 4511, 4512, 4518, 4519, 4520

Sun-Mack, S., Minnis, P., Chen, Y., Kato, S., Yi, Y., Gibson, S. C., Heck, P. W., and Winker, D. M.: Regional apparent boundary layer lapse rates determined from CALIPSO and MODIS data fro cloud height determination, J. Appl. Meteorol. Clim., 53, 990–1011, doi:10.1175/JAMC-D-13-081.1, 2014. 4509

Suttles, J. T., Wielicki, B. A., and Vemury, S.: Top-of-atmosphere radiative fluxes: validation of ERBE scanner inversion algorithm using Nimbus-7 ERB data, J. Appl. Meteorol., 31, 784–796, 1992. 4492

Wielicki, B. A., Barkstrom, B. R., Harrison, E. F., Lee, R. B., Smith, G. L., and Cooper, J. E.: Clouds and the Earth's Radiant Energy System (CERES): an earth observing system experiment, B. Am. Meteorol. Soc., 77, 853–868, 1996. 4491

Zhang, J. and Reid, J. S.: MODIS aerosol product analysis for data assimilation: assessment of over-ocean level 2 aerosol optical thickness retrievals, J. Geophys. Res., 111, D22207, doi:10.1029/2005JD006898, 2006. 4498

AMTD
8, 4489–4536, 2015

Table 1. Global mean TOA SW flux bias and RMS error by season derived from direct integration, using ADMs developed by Su et al. (2015) for the Edition 4 SSF data, and ADMs developed by Loeb et al. (2005) for the Edition 3 SSF data (shown in parentheses) for Terra 2002 and Aqua 2004.

	Terra 2002		Aqua 2004	
Season	Bias ($W m^{-2}$)	RMS ($W m^{-2}$)	Bias ($W m^{-2}$)	RMS ($W m^{-2}$)
Jan	0.04 (−0.28)	0.97 (1.19)	0.11 (−0.04)	1.00 (1.01)
Apr	0.08 (−0.10)	0.79 (0.98)	−0.16 (−0.23)	0.75 (1.03)
Jul	−0.20 (−0.42)	1.08 (1.45)	0.11 (−0.09)	0.90 (1.10)
Oct	0.02 (−0.16)	0.65 (0.81)	0.15 (−0.06)	0.78 (0.88)

AMTD
8, 4489–4536, 2015

Table 2. Regional mean TOA LW flux bias and RMS error by season derived from direct integration, using ADMs developed by Su et al. (2015) for the Edition 4 SSF data, and ADMs developed by Loeb et al. (2005) for the Edition 3 SSF data (shown in parentheses) for Terra 2002 and Aqua 2004.

	Terra 2002		Aqua 2004	
Season	Bias ($W m^{-2}$)	RMS ($W m^{-2}$)	Bias ($W m^{-2}$)	RMS ($W m^{-2}$)
Jan	0.37 (0.26)	0.72 (0.71)	0.29 (0.12)	0.64 (0.68)
Apr	0.47 (0.39)	0.76 (0.75)	0.37 (0.21)	0.60 (0.55)
Jul	0.44 (0.31)	0.78 (0.75)	0.31 (0.08)	0.71 (0.66)
Oct	0.39 (0.27)	0.65 (0.62)	0.36 (0.16)	0.61 (0.61)

AMTD
8, 4489–4536, 2015

Table 3. Regional mean TOA WN flux bias and RMS error by season derived from direct integration, using ADMs developed by Su et al. (2015) for the Edition 4 SSF data, and ADMs developed by Loeb et al. (2005) for the Edition 3 SSF data (shown in parentheses) for Terra 2002 and Aqua 2004.

	Terra 2002		Aqua 2004	
Season	Bias ($W m^{-2}$)	RMS ($W m^{-2}$)	Bias ($W m^{-2}$)	RMS ($W m^{-2}$)
Jan	0.19 (0.19)	0.30 (0.31)	0.18 (0.16)	0.29 (0.30)
Apr	0.24 (0.24)	0.34 (0.37)	0.21 (0.19)	0.29 (0.29)
Jul	0.23 (0.21)	0.35 (0.35)	0.19 (0.14)	0.31 (0.30)
Oct	0.20 (0.20)	0.29 (0.30)	0.22 (0.19)	0.30 (0.30)

AMTD
8, 4489–4536, 2015

Table 4. Cloud type classification used in TOA flux consistency tests. Each CERES footprint is assigned a scene identification index from 0 to 54 based upon cloud fraction (f, in %), mean effective cloud top pressure (EP), and cloud optical depth (τ), and whether one or two cloud layers are observed within the footprint. PCL: partly cloudy; MCL: mostly cloudy; and OVC: overcast.

		Clear	Partly cloudy			Mostly cloudy			Overcast		
			Thin	Mod.	Thick	Thin	Mod.	Thick	Thin	Mod.	Thick
Single Layer	High	0	19	20	21	22	23	24	25	26	27
	Mid		10	11	12	13	14	15	16	17	18
	Low		1	2	3	4	5	6	7	8	9
Multiple Layer	High	0	46	47	48	49	50	51	52	53	54
	Mid		37	38	39	40	41	42	43	44	45
	Low		28	29	30	31	32	33	34	35	36

Clear: $f \leq 0.1\,\%$
PCL: $0.1\,\% < f \leq 40\,\%$
MCL: $40\,\% < f \leq 99\,\%$
OVC: $99\,\% < f \leq 100\,\%$

Thin: $\tau \leq 3.35$
Moderate: $3.35 < \tau \leq 22.63$
Thick: $\tau > 22.63$

High: EP < 440 mb
Middle: $440\,\text{mb} \leq \text{EP} < 680\,\text{mb}$
Low: EP ≥ 680 mb

AMTD
8, 4489–4536, 2015

Table 5. TOA instantaneous footprint-level flux uncertainties ($W m^{-2}$) for SW flux, daytime and nighttime LW flux under clear-sky and all-sky conditions over three surface types based upon CERES MODIS flux consistency test.

	Ocean		Land		Snow/Ice	
	Clear	All	Clear	All	Clear	All
SW	2.0	9.0	5.8	9.7	5.3	10.7
LW Day	1.5	3.5	2.4	2.9	1.3	2.1
LW Night	1.4	2.0	1.2	1.9	1.4	1.4

AMTD
8, 4489–4536, 2015

Table 6. Flux consistency error due to ADM uncertainty using MISR measurements for clear-sky, single-layer cloud (S), multi-layer cloud (M), and all-sky conditions over three surface types. N is the minimum sample number required to derive the regression coefficients; Ψ_{ADM} is the relative consistency error due to ADM uncertainty before removing the parallax effect; Ψ_{PX} is the contribution of parallax effect to the total consistency error; Ψ'_{ADM} is the relative consistency error due to ADM uncertainty after removing the parallax effect.

		Ocean				Land				Snow/Ice			
		Clear	S	M	All	Clear	S	M	All	Clear	S	M	All
N		200	200	200	200	25	50	50	50	50	50	50	50
Ψ_{ADM}	(%)	3.5	4.6	8.4	6.2	2.0	4.9	6.6	4.0	3.8	6.0	6.1	5.6
Ψ_{PX}	(%)	0.0	2.2	2.8	2.3	0.0	2.7	3.4	0.9	0.0	0.7	0.0	0.0
Ψ'_{ADM}	(%)	3.5	4.1	7.9	5.8	2.0	4.1	5.7	3.9	3.8	6.0	6.1	5.6

AMTD
8, 4489–4536, 2015

Table 7. TOA instantaneous footprint-level SW flux uncertainties ($W m^{-2}$) under clear-sky, single-layer clouds, multi-layer clouds, and all-sky conditions over three surface types based upon MISR flux consistency test.

	Ocean	Land	Snow/Ice
Clear	1.8	3.2	6.7
Single	6.8	8.6	9.6
Multi	11.4	12.5	9.4
All	9.0	7.0	9.1

AMTD
8, 4489–4536, 2015

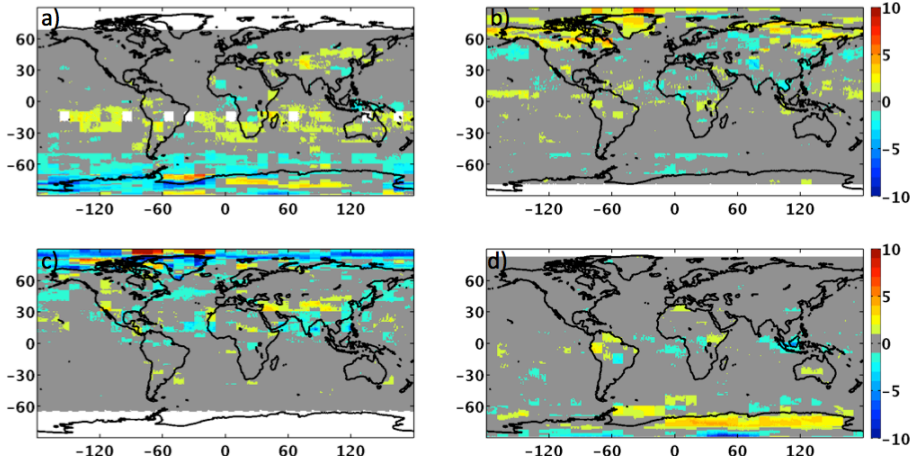

Figure 1. Monthly regional mean TOA shortwave flux error from ADM uncertainties for **(a)** January, **(b)** April, **(c)** July, and **(d)** October 2002 using Terra measurements.

AMTD
8, 4489–4536, 2015

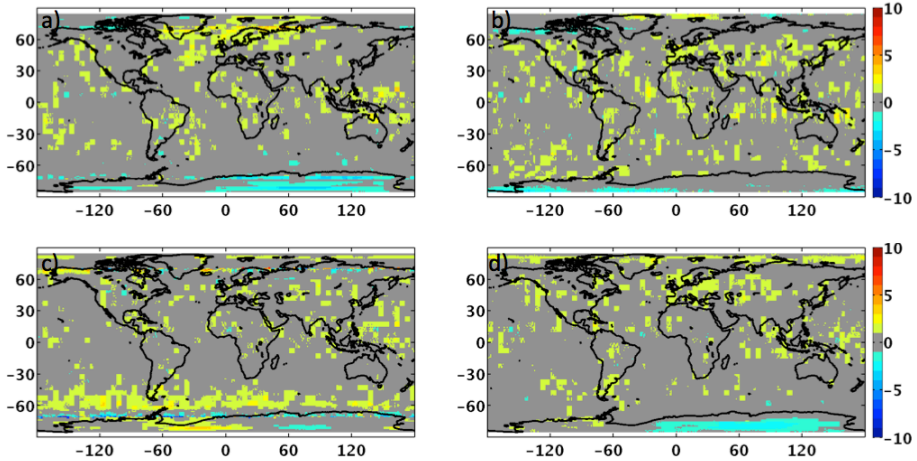

Figure 2. Monthly regional mean longwave flux error from ADM uncertainties for **(a)** January, **(b)** April, **(c)** July, and **(d)** October 2002 using Terra measurements.

AMTD
8, 4489–4536, 2015

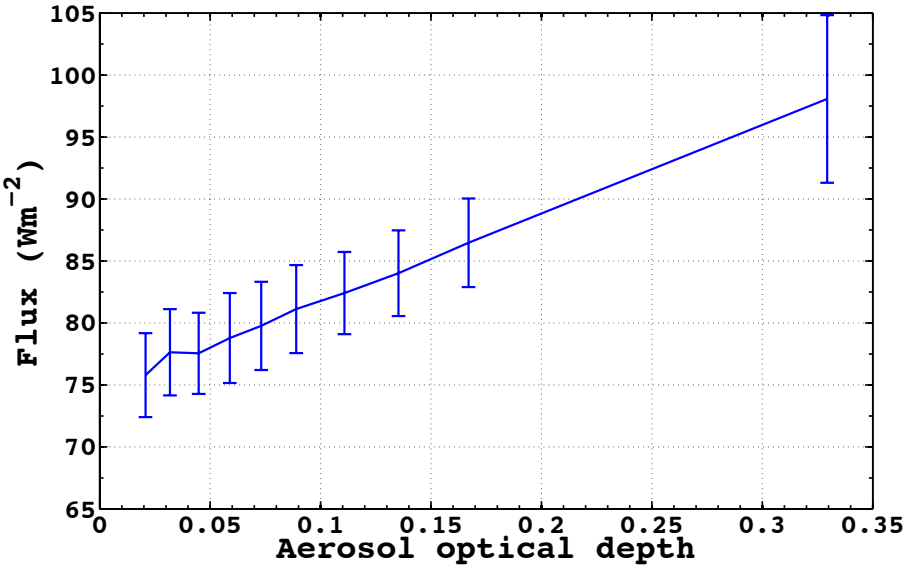

Figure 3. Mean oblique-view CERES fluxes and the relative RMS error (Eq. 3, in %) between oblique-view and near-nadir-view fluxes as a function of MODIS aerosol optical depth over clear ocean. The RMS errors are shown as error bars.

AMTD
8, 4489–4536, 2015

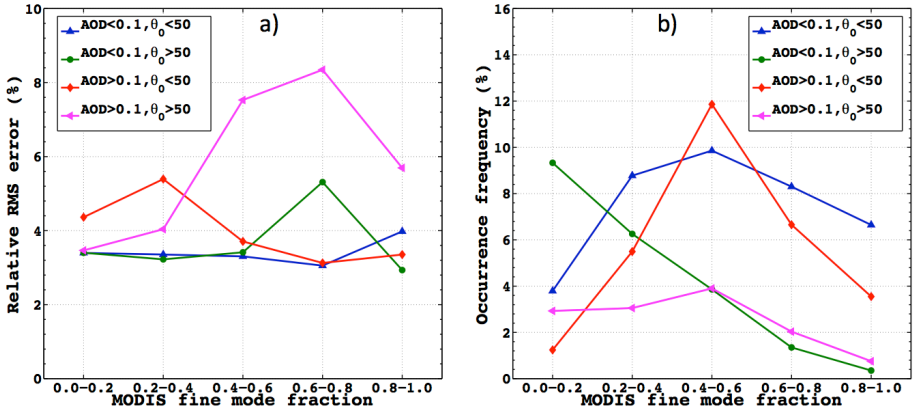

Figure 4. The relative RMS errors between oblique-view and near-nadir-view fluxes as a function of MODIS fine-mode fraction separated by aerosol optical depth (τ) of 0.1 and solar zenith angles (θ_0) of 50° **(a)**, and the occurrence frequency for each population **(b)**.

AMTD
8, 4489–4536, 2015

Validation of the next-generation angular distribution models

W. Su et al.

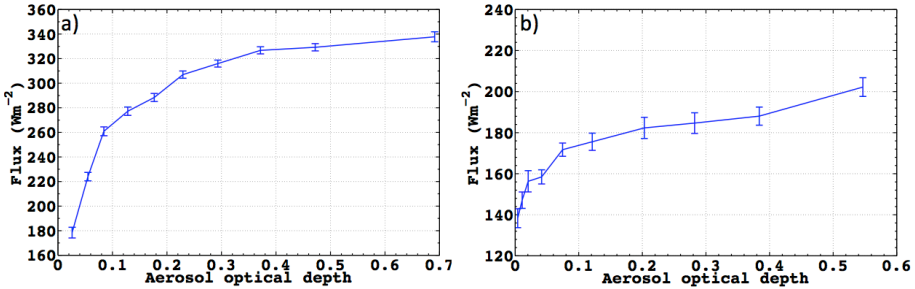

Figure 5. Mean oblique-view CERES fluxes and the relative RMS error (Eq. 3, in %) between oblique-view and near-nadir-view fluxes as a function of MODIS aerosol optical depth **(a)** over clear land and **(b)** clear Amazon (0–30° S, 40–80° W). The RMS errors are shown as error bars.

AMTD
8, 4489–4536, 2015

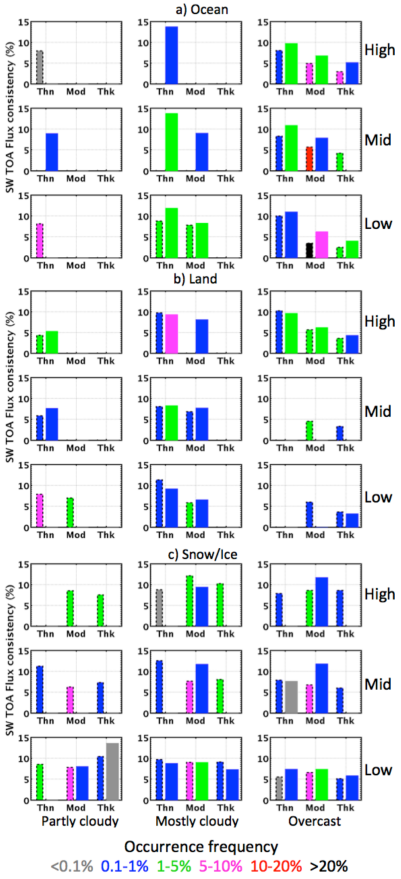

Figure 6. TOA SW flux consistency error (%) between nadir- and oblique-viewing angles for different cloud types over **(a)** ocean, **(b)** land, and **(c)** snow and ice. The left bars (narrow) are for single layer clouds and the right bars (wide) are for multiple layer clouds. The color of the bar indicates the occurrence frequency for each cloud type.

AMTD
8, 4489–4536, 2015

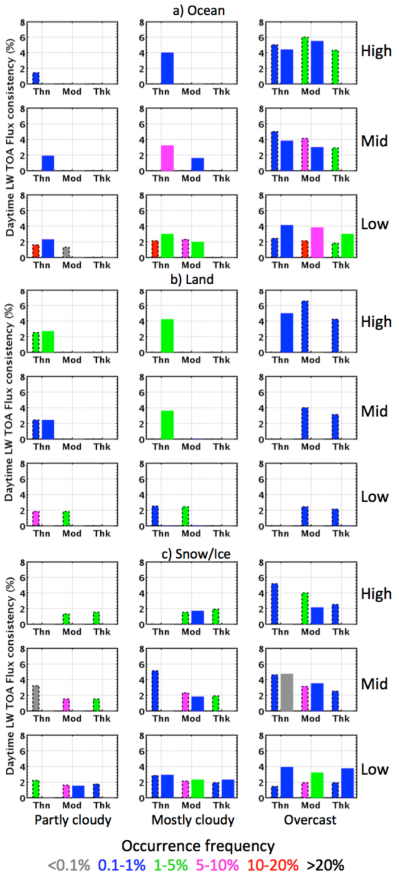

Figure 7. TOA daytime LW flux consistency error (%) between nadir- and oblique-viewing angles for different cloud types over **(a)** ocean, **(b)** land, and **(c)** snow and ice. The left bars (narrow) are for single layer clouds and the right bars (wide) are for multiple layer clouds. The color of the bar indicates the occurrence frequency for each cloud type.

AMTD
8, 4489–4536, 2015

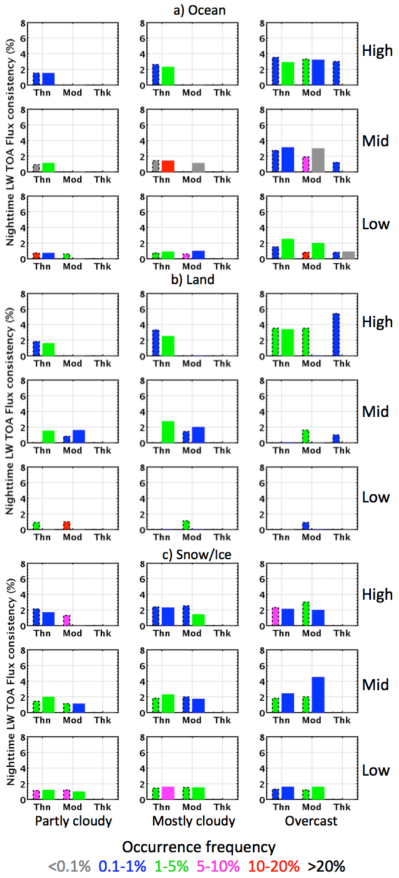

Figure 8. TOA nighttime LW flux consistency error (%) between nadir- and oblique-viewing angles for different cloud types over **(a)** ocean, **(b)** land, and **(c)** snow and ice. The left bars (narrow) are for single layer clouds and the right bars (wide) are for multiple layer clouds. The color of the bar indicates the occurrence frequency for each cloud type.

AMTD
8, 4489–4536, 2015

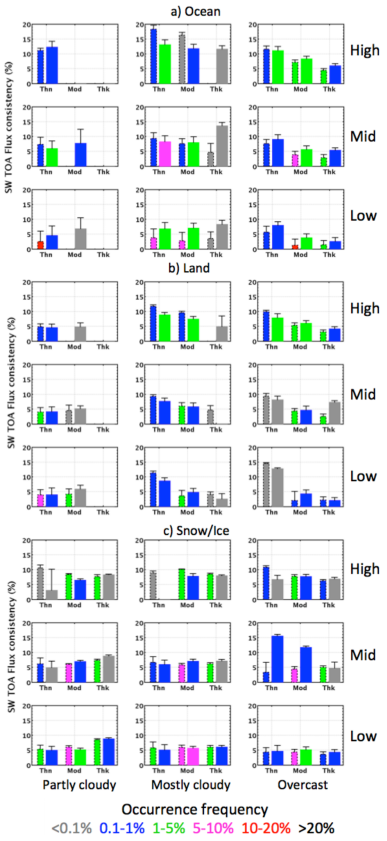

Figure 9. TOA SW flux consistency error (%) among the MISR camera angles for different cloud types over **(a)** ocean, **(b)** land, and **(c)** snow and ice. The height of the bar shows the flux consistency error due to ADM uncertainties and the error bar shows the contribution of narrowband-to-broadband regression to the total consistency error. The left bars (narrow) are for single layer clouds and the right bars (wide) are for multiple layer clouds. The color of the bar indicates the occurrence frequency for each cloud type

AMTD
8, 4489–4536, 2015

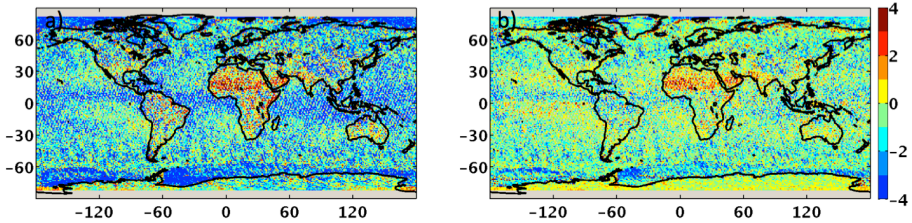

Figure 10. TOA SW flux error ($W m^{-2}$) caused by scene identification uncertainty (standard – enhanced) **(a)** only using near-nadir viewing geometries, **(b)** using extended viewing geometries that are similar to the CERES observations.

AMTD
8, 4489–4536, 2015

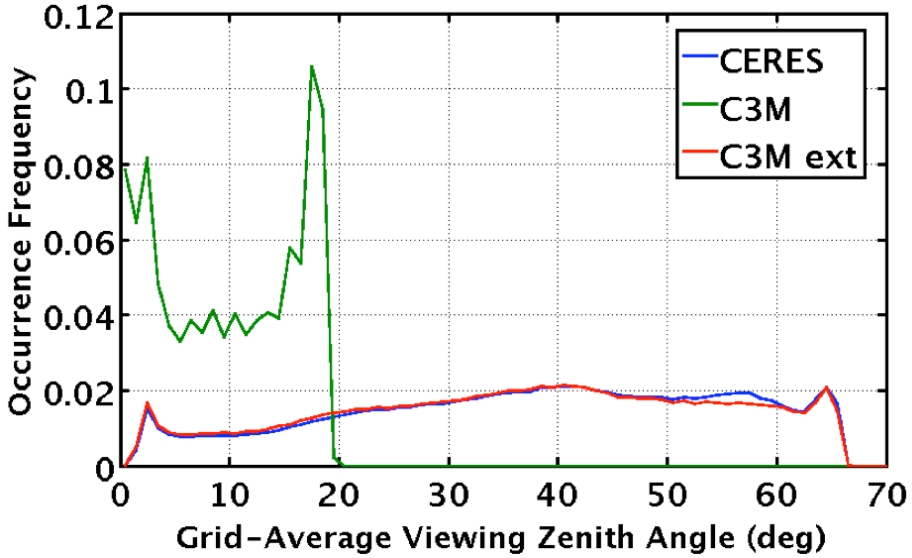

Figure 11. Distributions of grid-averaged viewing zenith angle for CERES data (blue), C3M data (green), and the C3M extended data (red), using data of April 2010.

AMTD
8, 4489–4536, 2015

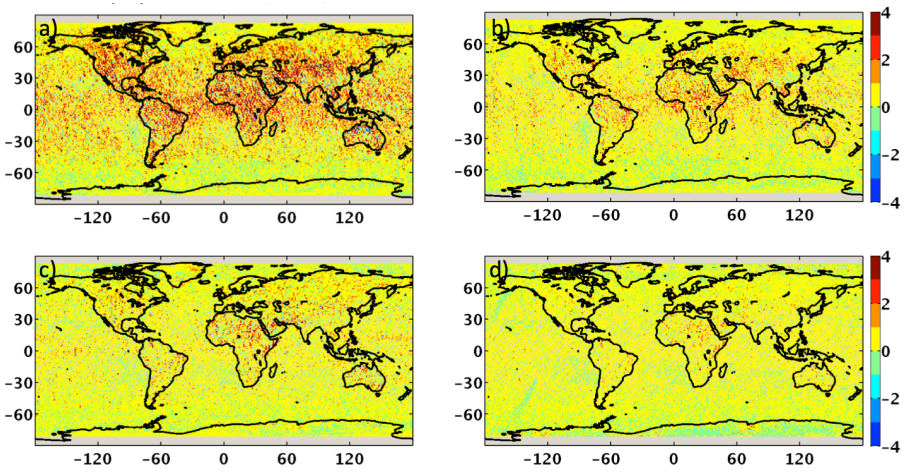

Figure 12. TOA LW flux error ($W m^{-2}$) caused by scene identification uncertainty (standard – enhanced) **(a)** daytime LW flux error only using near-nadir viewing geometries, **(b)** daytime LW flux error using extended viewing geometries that are similar to the CERES observations, **(c)** same as **(a)** but for nighttime LW flux error, **(d)** same as **(b)** but for nighttime LW flux error.

AMTD
8, 4489–4536, 2015